

# Generation of Twisted Gamma-Rays via Two-Photon Transition

Motomichi Tashiro<sup>1</sup>, Noboru Sasao<sup>2</sup> and Minoru Tanaka<sup>3</sup>

<sup>1</sup> Department of Applied Chemistry, Toyo University, Kawagoe, Saitama 350-8585, Japan

<sup>2</sup> Research Institute for Interdisciplinary Science, Okayama University, Okayama 700-8530, Japan

<sup>3</sup> Graduate School of Science, Osaka University, Toyonaka, Osaka 560-0043, Japan

E-mail: sasao@okayama-u.ac.jp

March 2022

**Abstract.** We present a new and efficient method of generating twisted gamma rays utilizing highly accelerated helium-like ions; they are excited to a chosen state by irradiating two optical lasers and emit a photon with orbital angular momentum in the deexcitation process. We study its emission rate together with other properties such as background and photo-ionization processes.

## 1. Introduction

Light or, its quantum, photon is characterized by the linear momentum (or wave vector) and the helicity in the case of plane wave. It is also possible to describe the photon in terms of the multipole field specified by the energy, the total angular momentum  $J_\gamma$  and its projection  $M_\gamma$  onto a quantization axis [1]. Then, one may say that a photon has an orbital angular momentum (OAM) as well as the spin angular momentum if  $J_\gamma \geq 2$ .

In the form of propagating beam, light with OAM is realized by the Laguerre-Gaussian beam, which solves the wave equation in the paraxial approximation, as Allen et al. discovered in 1992 [2]. The wave front of such a beam is a helicoid, exhibiting a phase singularity and a complete dark spot along the beam axis, thus mentioned as “twisted” or “vortex” in the literature. The OAM degree of freedom of twisted photons has provided a fresh view of the light-matter interaction and novel applications [3, 4, 5, 6]. The range of applications is wide, including fundamental interaction between atoms and photons [7, 8], quantum optics [9, 10], micro manipulation of particles/materials [11, 12], microscopy and imaging [13, 14, 15], optical data transmission [16, 17, 18], and astrophysics [19, 20, 21].

Fork holograms, spiral phase plates [22], lens-based mode converters [23] and q-plates [24] are popular methods employed to generate optical beams with OAM. As for the X-ray region, high-harmonic radiation from a helical undulator [25, 26, 27],

and coherent emission from spirally-bunched electrons produced by combination of a laser and undulator [28, 29, 30] are apparently promising. Proposed methods to generate twisted gamma rays fall into two classes depending on the method of energy up-conversion: Backward Compton scattering [31, 32, 33, 34, 35, 36, 37], and photon absorption-emission by accelerated partially stripped ions (PSIs) [38, 39, 40]. The proposed gamma factory [41, 42] is supposed for the latter scenario. Compared with the backward Compton scattering, the latter process has an advantage of having much bigger fundamental cross section; the Rayleigh scattering cross section proportional to square of the resonant wavelength versus the Thomson scattering cross section proportional to square of the classical electron radius. Beams of twisted gamma rays are expected to be useful in the studies of nuclear structure, spin puzzle of nucleons [43], and astrophysical phenomena associated with rotation and/or strong magnetic field.

In ref. [39], a method to generate twisted photons using hydrogen-like (H-like) ions is studied. A laser beam of twisted photons in the visible region is irradiated to a bunch of accelerated H-like ions. The laser energy is chosen to excite the ground state  $1s_{1/2}$  to the excited state  $3d_{5/2}(m = 5/2)$ . When the excited state goes back to the ground state via the electric quadrupole (E2) transition, a twisted photon of  $(J_\gamma, M_\gamma) = (2, 2)$  is emitted as described above. The energy of the emitted twisted photons is up-converted by a factor of  $4\gamma_{ion}^2$  from the irradiated optical twisted laser, where  $\gamma_{ion}$  represents the Lorentz boost factor of ions and the case of  $\gamma_{ion} \gg 1$  is considered. The emitted photons are also highly collimated along the direction of the ion's motion.

Although the expected flux of twisted photons in this method is sizable, a potential problem is background. One of the major backgrounds is the electric dipole (E1) transition from  $3d_{5/2}$  to  $2p_{3/2}$ . The E1 rate is much larger than the signal E2 rate though the energy of the background photons is fairly different from the signal. Another background is the E2 photon of  $M_\gamma = 1$  from  $3d_{5/2}(m = 3/2)$ . This photon does not exhibit the phase singularity nor the dark spot along the ion boost axis contrary to the one with  $M_\gamma = 2$ . It is possible in principle to suppress this background by applying a transverse magnetic field to make the Zeeman splitting and selecting the energy of the irradiating twisted laser beam so that the excitation to  $3d_{5/2}(m = 3/2)$  does not occur. This method of background suppression leads to more complication in the design of the collision point of the gamma factory than usual.

In this article, we present a new and efficient method of generating twisted gamma rays utilizing highly accelerated ( $\gamma_{ion} \gg 1$ ) helium-like (He-like) PSIs; an accelerated He-like PSI is excited to a chosen state by irradiating two non-twisted optical lasers and emits a photon with OAM in the deexcitation process. The energies of two laser photons seen by the ions are blue-shifted by a factor of  $2\gamma_{ion}$ , and then the energy of photons emitted in the backward (ion-boost) direction is  $2\gamma_{ion}$  times the chosen level splitting of the ion at rest. A salient feature of the proposed method is to utilize a decay process from an excited state with an angular momentum  $J = 2$ ,  $M = \pm 2$  back to the ground state of  $J = 0$ ,  $M = 0$ . In order to reach the excited state with  $J = 2$ ,  $M = \pm 2$ , two-photon STIRAP (STImulated Raman Adiabatic Passage) [44] is employed. We examine

backgrounds and the ion loss by photo-ionization as well as the signal rate, and argue that they are not harmful.

This paper is organized as follows. In the next section, we present a basic theory of the method, including its principle, calculation of ion properties and STIRAP method. The goal in this section is to provide the framework of the temporal evolution of a He-like PSI under the irradiation of laser pulses. In section 3, we present the results of our calculations, and discuss about signal, backgrounds, and the photoionization. In section 4, summary is given together with discussions. Some details are relegated to the appendix.

Throughout this paper, we use the SI unit system unless otherwise noted, and as usual,  $c$ ,  $\hbar$ ,  $e$  and  $m_e$  denote the light velocity in vacuum, the reduced Plank constant, the unit charge, and the electron mass, respectively.

## 2. Theory

### 2.1. Principle of generating twisted gamma-rays

As stated already, we utilize high-energy He-like ions as an energy converter. For clarity, we assume that the ions are accelerated and/or stored in a circular ring up to the Lorentz boost factor of  $\gamma_{ion}$ . A schematic energy diagram of He-like ions is shown in Figure 1. Let's suppose that ions are populated in a  $|2^3P_2\rangle$  state with a total angular momentum  $J = 2$  and its magnetic quantum number  $M = 2$  along the beam direction. Here the state is specified by a standard symbol of the LS-coupling scheme,  $^{2S+1}L_J$ , and the principal quantum number  $n = 2$  attached in front. They decay back to the ground state by emitting a photon with an angular momentum of 2. For a sufficiently large  $\gamma_{ion}$ , say  $> 1000$ , the energy of emitted photon is amplified to a gamma ray region in a laboratory. One crucial feature of He-like ions is that the transition from  $|2^3P_2\rangle$  to the ground state, magnetic quadrupole (M2) in nature, is a major decay channel. This is due to a relativistic effect: the M2 transition is expected to scale with  $Z^8$ , which becomes sizable when high  $Z$  ions are selected [45, 46]. The STIRAP method, in which two circularly polarized lasers are irradiated to populate the  $J = 2$  and  $M = 2$  states, is used for an efficient transition. This is the basic principle of generating gamma-rays with OAM. Below we consider He-like Kr ( $Z = 36$ ) with  $\gamma_{ion} = 2500$  and Xe ( $Z = 54$ ) with  $\gamma_{ion} = 5000$  as an illustration. Gamma-rays with energies of  $\sim 65$  MeV (Kr) or  $\sim 306$  MeV (Xe) are obtained for  $\gamma_{ion}$  chosen above. Similar discussions and/or conclusions apply equally to other He-like ions.

### 2.2. Properties of He-like ions—Details of calculations—

#### *Energy levels and radiative transitions*

In this work, energy levels of He-like Kr and Xe were calculated by the multi-configuration Dirac-Hartree-Fock method and the relativistic configuration interaction method [47] implemented in the GRASP2018 package [48]. The wave functions for

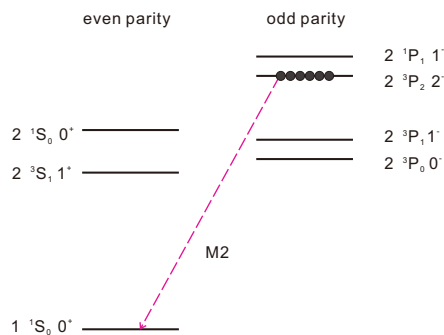


Figure 1: Schematic diagram of He-like ion energy levels. Symbols of LS-coupling scheme,  $n^{2S+1}L_J J^\pm$ , are used. Populations in  $2\ ^3P_2$  levels decay to the ground state via M2 transition. Not to scale.

these atomic states were represented by linear combinations of configuration state functions, which were constructed from single-particle Dirac orbitals. The single-particle Dirac orbitals were determined by the multi-configuration Dirac-Hartree-Fock method, whereas the expansion coefficients of the linear combination were calculated by the relativistic configuration interaction method. Using the multi-configuration Dirac-Hartree-Fock method, single-particle Dirac orbitals were obtained up to  $7s, 7p, 7d, 6f$  and  $6g$ . Treating these orbitals as active space, the relativistic configuration interaction calculations were performed to include the Breit interaction [47], vacuum polarization [49], and self-energy [49] effects. Total of 17 electronic states as well as the amplitudes of the E1, E2, M1 and M2 transitions among these states were calculated in this work. The results of calculations are summarized in Table 1, and are illustrated in Figure 2.

Label	State	He-like Kr		He-like Xe	
		Energy /eV	$\tau$ /s	Energy /eV	$\tau$ /s
$ g\rangle$	$1\ 0^+ 1s(0)\ ^1S_0$	0.000	-	0.000	-
$ 1\rangle$	$1\ 1^+ 1s\ 2s\ ^3S_1$	12978.4	$1.749 \times 10^{-10}$	30127.3	$2.627 \times 10^{-12}$
$ 5\rangle$	$1\ 0^- 1s\ 2p\ ^3P_0^o$	13022.5	$1.456 \times 10^{-9}$	30210.3	$5.836 \times 10^{-10}$
$ 3\rangle$	$1\ 1^- 1s\ 2p\ ^3P_1^o$	13025.2	$2.540 \times 10^{-15}$	30204.3	$3.270 \times 10^{-16}$
$ 4\rangle$	$2\ 0^+ 1s\ 2s\ ^1S_0$	13025.9	$1.173 \times 10^{-5}$	30212.8	$8.098 \times 10^{-7}$
$ f\rangle$	$1\ 2^- 1s\ 2p\ ^3P_2^o$	13089.9	$9.571 \times 10^{-12}$	30592.8	$3.458 \times 10^{-13}$
$ 2\rangle$	$2\ 1^- 1s\ 2p\ ^1P_1^o$	13113.7	$6.551 \times 10^{-16}$	30628.0	$1.471 \times 10^{-16}$
$ e\rangle$	$2\ 1^+ 1s\ 3s\ ^3S_1$	15394.4	$8.400 \times 10^{-14}$	35821.1	$1.396 \times 10^{-14}$
	$3\ 0^+ 1s\ 3s\ ^1S_0$	15407.0	$8.929 \times 10^{-14}$	35843.8	$1.462 \times 10^{-14}$
	$2\ 0^- 1s\ 3p\ ^3P_0^o$	15407.1	$2.846 \times 10^{-14}$	35844.3	$1.008 \times 10^{-15}$
	$3\ 1^- 1s\ 3p\ ^3P_1^o$	15407.8	$6.969 \times 10^{-15}$	35845.8	$5.077 \times 10^{-15}$
	$2\ 2^- 1s\ 3p\ ^3P_2^o$	15427.1	$3.038 \times 10^{-14}$	35959.6	$5.937 \times 10^{-15}$
	$1\ 2^+ 1s\ 3d\ ^3D_2$	15433.0	$9.942 \times 10^{-15}$	35968.3	$1.818 \times 10^{-15}$
	$3\ 1^+ 1s\ 3d\ ^3D_1$	15433.4	$9.986 \times 10^{-15}$	35969.7	$4.821 \times 10^{-16}$

$4\ 1^- 1s\ 3p\ ^1P_1^o$	15434.6	$2.232 \times 10^{-15}$	35969.8	$1.850 \times 10^{-15}$
$1\ 3^+ 1s\ 3d\ ^3D_3$	15439.7	$1.023 \times 10^{-14}$	36004.5	$1.955 \times 10^{-15}$
$2\ 2^+ 1s\ 3d\ ^1D_2$	15440.3	$1.019 \times 10^{-14}$	36005.9	$1.915 \times 10^{-15}$

Table 1: Low-lying levels of He-like Kr and Xe, and their energies and lifetimes. Ascending order in energy except  $|3\rangle$  and  $|5\rangle$  of Xe. The states  $|i\rangle$  ( $i = g, e, f, 1 \dots 5$ ) are considered in the simulation study.

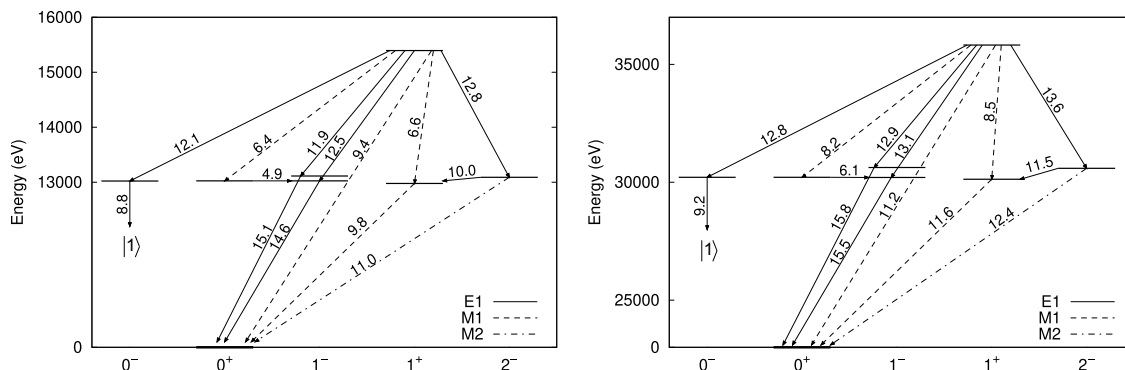


Figure 2: Low-lying energy levels of He-like Kr (left) and Xe (right). Major radiative transitions are indicated by arrows (E1 by solid, M1 by dashed, and M2 by dash-dotted lines) together with A-coefficients (powers of 10).

### Photo-ionization cross section

To estimate the fraction of ionization caused by the laser used in the experiment, photoionization cross sections of He-like ions were calculated by using the RATIP programs[50]. The wavefunctions of the ions used in the photoionization calculation were basically the same as described just above. The results of calculations, relevant to our present studies, are summarized in Table 2.

### 2.3. Population transfer by Raman process

The technique of stimulated Raman adiabatic passage (STIRAP) is now a well established one: it allows efficient and selective population transfer between quantum states without suffering loss due to spontaneous emission [44]. As illustrated by the thick solid arrows in Figure 3, two lasers (pump and Stokes) are irradiated to stimulate transitions from the ground state  $|g\rangle = |1\ ^1S_0\rangle$  to the final state  $|f\rangle = |2\ ^3P_2\rangle$  via the

Table 2: Photo-ionization Cross-section

Symbol	Initial state	He-like Kr		He-like Xe	
		$\hbar\omega/\text{eV}$	$\sigma^{(pi)}/\text{barn}$	$\hbar\omega/\text{eV}$	$\sigma^{(pi)}/\text{barn}$
$\sigma_{es}^{(pi)}$	$2\ 1^+ 1s\ 3s\ ^3S_1$	2304.5	15330	5228.3	6839
$\sigma_{ep}^{(pi)}$	$2\ 1^+ 1s\ 3s\ ^3S_1$	15394.4	203.0	35821.1	84.78
$\sigma_{fp}^{(pi)}$	$1\ 2^- 1s\ 2p\ ^3P_2^o$	15394.4	90.78	35821.1	36.60
$\sigma_{1p}^{(pi)}$	$1\ 1^+ 1s\ 2s\ ^3S_1$	15394.4	709.7	35821.1	292.8
$\sigma_{2p}^{(pi)}$	$2\ 1^- 1s\ 2p\ ^1P_1^o$	15394.4	139.2	35821.1	57.22
$\sigma_{3p}^{(pi)}$	$1\ 1^- 1s\ 2p\ ^3P_1^o$	15394.4	148.4	35821.1	70.74
$\sigma_{4p}^{(pi)}$	$2\ 0^+ 1s\ 2s\ ^1S_0$	15394.4	747.1	35821.1	311.2
$\sigma_{5p}^{(pi)}$	$1\ 0^- 1s\ 2p\ ^3P_0^o$	15394.4	206.6	35821.1	97.29

excited state  $|e\rangle = |3^3S_1\rangle$ . The Hamiltonian for the process is given by

$$H(t) = \hbar \begin{bmatrix} 0 & \frac{1}{2}\Omega_P & 0 \\ \frac{1}{2}\Omega_P^* & -\Delta & \frac{1}{2}\Omega_S^* \\ 0 & \frac{1}{2}\Omega_S & -\delta \end{bmatrix} \quad (1)$$

after applying the rotating wave approximation [44]. Here  $\Omega_P$  and  $\Omega_S$  denote Rabi frequencies of pump and Stokes laser fields, respectively, and  $\Delta$  ( $\delta$ ) is the pump laser detuning (two-photon detuning) defined as

$$\Delta \equiv \omega_p - \omega_{eg}, \quad \delta \equiv \omega_p - \omega_s - \omega_{fg} \quad (2)$$

where  $\omega_p$  ( $\omega_s$ ) is the pump (Stokes) laser frequency, and  $\hbar\omega_{eg}$  ( $\hbar\omega_{fg}$ ) is the  $|e\rangle - |g\rangle$  ( $|f\rangle - |g\rangle$ ) energy difference. The Rabi frequencies are calculated with respective A-coefficients and are specified in more detail below. In addition to the Raman process, processes such as spontaneous decay or photo-ionization are of practical importance. To study their effects, all  $n = 2$  states, labeled as  $|1\rangle \sim |5\rangle$  in Figure 3, are considered in the simulation described below. See Table 1 for the actual assignment. These states are populated by the spontaneous emission from the excited state  $|e\rangle$  (and less importantly from higher levels within  $n = 2$ ), and generate background gamma-rays with energies similar to the signal by decaying to the ground state  $|g\rangle$ .

### Optical Bloch equations

In order to examine population transfer efficiency, we employ optical Bloch equations, in which effects of all major decays are taken into account based on the master equation[51]. The optical Bloch equations (in the ion-rest frame) are given by

$$\begin{aligned} \frac{d\rho_{gg}}{dt} &= -\Re\left(i\Omega_P\rho_{ge}^*\right) + \sum_{j=e,f}^{1\sim 5} \Gamma_{jg}\rho_{jj} \\ \frac{d\rho_{ee}}{dt} &= +\Re\left(i\Omega_P\rho_{ge}^* + i\Omega_S\rho_{fe}^*\right) - \left(\Gamma_e^{(tot)} + \Gamma_e^{(pi)}\right)\rho_{11} \end{aligned}$$

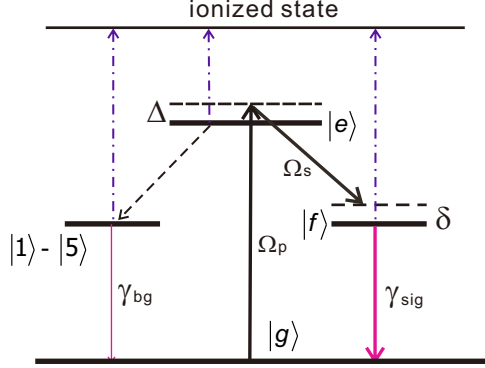


Figure 3: Levels and processes relevant to the STIRAP simulation. The major levels are  $|g\rangle = |1^1S_0\rangle$ ,  $|e\rangle = |3^3S_1\rangle$ , and  $|f\rangle = |2^3P_2\rangle$ . The thick solid arrows indicate the main path for generating  $\gamma_{sig}$ .  $\Omega_p(\Omega_s)$  denotes Rabi frequency of the pump (Stokes) laser, and  $\Delta$  ( $\delta$ ) is pump laser (two-photon) detuning. The dashed line represents the spontaneous radiative decays and the dash-dotted ones indicate photo-ionization processes. See Table 1 for the levels labeled by Arabic numerals.

$$\begin{aligned}
 \frac{d\rho_{ff}}{dt} &= -\Re\left(i\Omega_s\rho_{fe}^*\right) + \Gamma_{ef}\rho_{ee} - \left(\Gamma_f^{(tot)} + \Gamma_f^{(pi)}\right)\rho_{ff} \\
 \frac{d\rho_{ge}}{dt} + i\Delta\rho_{ge} &= \frac{i}{2}\left(\Omega_s\rho_{gf} + \Omega_p(\rho_{gg} - \rho_{ee})\right) - \gamma_{ge}\rho_{ge} \\
 \frac{d\rho_{gf}}{dt} + i\delta\rho_{gf} &= \frac{i}{2}\left(\Omega_s^*\rho_{ge} - \Omega_p\rho_{fe}^*\right) - \gamma_{gf}\rho_{gf} \\
 \frac{d\rho_{fe}}{dt} + i(\Delta - \delta)\rho_{fe} &= \frac{i}{2}\left(\Omega_p\rho_{gf}^* + \Omega_s(\rho_{ff} - \rho_{ee})\right) - \gamma_{fe}\rho_{fe} \\
 \frac{d\rho_{ii}}{dt} &= \left(\Gamma_{ei}\rho_{ee} + \Gamma_{ji}\rho_{jj}\right) - \left(\Gamma_{ig} + \Gamma_{ij} + \Gamma_i^{(pi)}\right)\rho_{ii}, \quad (i, j) = (1, \dots, 5) \quad (3)
 \end{aligned}$$

where  $\rho_{ii}$  ( $\rho_{ij}$ ) denotes the population of the state  $|i\rangle$  (coherence between  $|i\rangle$  and  $|j\rangle$ ), and  $\Gamma_i^{(tot)}$  ( $\Gamma_{ij}$ ) is the corresponding total (partial) width. The actual values of  $1/\Gamma_i^{(tot)}$  (*i.e.* lifetime) and  $\Gamma_{ij}$  are specified in Table 1 or in Table 4. Using Equation (9) in Appendix, the Rabi frequencies are given by

$$\begin{aligned}
 \Omega_p(t) &= \frac{eE_p(t)}{\hbar} \sqrt{\frac{3\Gamma_{eg}}{4\alpha k_p^3}}, \\
 \Omega_s(t) &= \frac{eE_s(t)}{\hbar} \sqrt{\frac{9\Gamma_{ef}}{20\alpha k_s^3}}, \quad (4)
 \end{aligned}$$

where  $E_p$  ( $E_s$ ) denotes the magnitude of the pump (Stokes) laser field with wavenumber  $k_p$  ( $k_s$ ) and  $\alpha \simeq 1/137$  is the fine structure constant. Table 3 shows the Rabi frequencies for an unit input power  $I_{in} = 1$  W/mm<sup>2</sup>. As seen, there is a large imbalance between  $\Omega_p$  and  $\Omega_s$ .

The transverse decay (decoherence) are assumed to stem from longitudinal

components and their constants are taken as follows:

$$\begin{aligned}\gamma_{ge} &= \frac{1}{2}\Gamma_e^{(tot)}, & \gamma_{gf} &= \frac{1}{2}\Gamma_f^{(tot)} \\ \gamma_{fe} &= \frac{1}{2}\left(\Gamma_e^{(tot)} + \Gamma_f^{(tot)}\right).\end{aligned}\quad (5)$$

The terms  $\Gamma_i^{(pi)}$  ( $i = e, f, 1, \dots, 5$ ) need special attention. These terms represent a photo-ionization effect due to absorption of additional laser photons. The ionization rate is expressed by

$$\begin{aligned}\Gamma_e^{(pi)} &= \sigma_{es}^{(pi)} \frac{I_s(t)}{\hbar\omega_s} + \sigma_{ep}^{(pi)} \frac{I_p(t)}{\hbar\omega_p}, \\ \Gamma_i^{(pi)} &= \sigma_{ip}^{(pi)} \frac{I_p(t)}{\hbar\omega_p} \quad (i = f, 1, \dots, 5),\end{aligned}\quad (6)$$

where  $\sigma_{ip}^{(pi)}$  or  $\sigma_{is}^{(pi)}$  denotes the photo-ionization cross-section of the state  $|i\rangle$  by pump or Stokes lasers,  $I_{p,s}(t)$  the laser intensity, and  $\frac{I_{p,s}(t)}{\hbar\omega_{p,s}}$  the photon number flux ( $\omega_{p,s} = ck_{p,s}$ ). We note that the energy of Stokes laser photons is below the photo-ionization threshold except for  $|e\rangle$ . We also note that since  $|e\rangle$  is the lowest among the  $n = 3$  states, there is no decay path going through them.

Table 3: Rabi frequency for unit input power  $I_{in} = 1$  W/mm<sup>2</sup> (in the ion-at-rest frame).

Transitions	Type	Kr [s <sup>-1</sup> ]	Xe [s <sup>-1</sup> ]
$\Omega_p \quad  g\rangle \rightarrow  e\rangle$	M1	$5.570 \times 10^4$	$1.276 \times 10^5$
$\Omega_s \quad  e\rangle \rightarrow  f\rangle$	E1	$3.935 \times 10^7$	$2.882 \times 10^7$

### 3. Simulation Results

#### 3.1. Overview of the simulation results

We first describe a basic parameter set used in the simulation. See Table 5 (note that values are all in the laboratory frame). The Lorentz boost factor  $\gamma_{ion}$  is assumed to be  $\gamma_{ion} = 2500$  for Kr and  $\gamma_{ion} = 5000$  for Xe. These choices are made so that wavelengths of input lasers fall into a convenient region (visible or infrared). Assuming that an ion beam has a bunching time structure in a ring accelerator, we use pulsed lasers for both pump and Stokes. The time profiles are assumed to be Gaussian, and are expressed by

$$I_{p,s}(t) = I_{p,s}(0) \exp\left(-\frac{(t \mp t_d)^2}{2\sigma_L^2}\right), \quad (7)$$

where  $\sigma_L$  denotes a root-mean-square width and  $t_d$  a time difference between the two pulses (the Stokes precedes the pump by  $2t_d$ ). We call  $t_d$  a laser delay time for convenience. The width  $\sigma_L$  and delay time  $t_d$  are taken to be 1 nsec and 0.5 nsec,



Table 4: Radiative transitions used in the simulation

Transitions	Type	He-like Kr		He-like Xe	
		Energy/eV	$\Gamma/s^{-1}$	Energy/eV	$\Gamma/s^{-1}$
$ e\rangle \rightarrow  g\rangle$	M1	15394	$2.469 \times 10^9$	35821	$1.633 \times 10^{11}$
$ e\rangle \rightarrow  f\rangle$	E1	2305	$6.891 \times 10^{12}$	5228	$4.317 \times 10^{13}$
$ e\rangle \rightarrow  1\rangle$	M1	2416	$4.066 \times 10^6$	5694	$2.936 \times 10^8$
$ e\rangle \rightarrow  2\rangle$	E1	2281	$8.444 \times 10^{11}$	5193	$7.705 \times 10^{12}$
$ e\rangle \rightarrow  3\rangle$	E1	2369	$2.927 \times 10^{12}$	5617	$1.388 \times 10^{13}$
$ e\rangle \rightarrow  4\rangle$	M1	2369	$2.289 \times 10^6$	5608	$1.603 \times 10^8$
$ e\rangle \rightarrow  5\rangle$	E1	2372	$1.241 \times 10^{12}$	5611	$6.701 \times 10^{12}$
$ f\rangle \rightarrow  g\rangle$	M2	13090	$9.309 \times 10^{10}$	30593	$2.554 \times 10^{12}$
$ 1\rangle \rightarrow  g\rangle$	M1	12978	$5.719 \times 10^9$	30127	$3.806 \times 10^{11}$
$ 2\rangle \rightarrow  g\rangle$	E1	13114	$1.526 \times 10^{15}$	30628	$6.798 \times 10^{15}$
$ 3\rangle \rightarrow  g\rangle$	E1	13025	$3.936 \times 10^{14}$	30204	$3.058 \times 10^{15}$
$ f\rangle \rightarrow  1\rangle$	E1	112	$1.139 \times 10^{10}$	465	$3.374 \times 10^{11}$
$ 4\rangle \rightarrow  3\rangle$	E1	13026	$8.385 \times 10^4$	30213	$1.192 \times 10^6$
$ 5\rangle \rightarrow  1\rangle$	E1	0.7	$6.866 \times 10^8$	8.5	$1.714 \times 10^9$

respectively. The peak intensity  $I_p(0)$  and  $I_s(0)$  are assumed to be equal and are 400 kW/mm<sup>2</sup>. With the laser spot size of 1 mm<sup>2</sup>, the laser's total pulse energies amount to 1 mJ per pulse for each. The pump laser detuning  $\Delta$  is taken to be 5 times  $\Gamma_e^{(tot)}$ , and the two-photon detuning is set to  $\delta = 0$ . The Rabi frequency profiles, calculated according to Equation (4) are shown in Figure 4. In the following section, we assume the transverse ion beam size matches with the laser spot size (*i.e.* less than 1 mm<sup>2</sup>).

Table 5: Basic parameter set used in the simulation.

Parameter	Symbol	Kr	Xe	units
Lorentz boost factor	$\gamma_{ion}$	2500	5000	-
Pump laser wavelength	$\lambda_p$	403	346	nm
Pump laser intensity	$I_p(0)$	$4 \times 10^5$	$4 \times 10^5$	W/mm <sup>2</sup>
Stokes laser wavelength	$\lambda_s$	2690	2371	nm
Stokes laser intensity	$I_s(0)$	$4 \times 10^5$	$4 \times 10^5$	W/mm <sup>2</sup>
Laser pulse width	$\sigma_L$	1.0	1.0	nsec
Laser pulse delay	$t_d$	0.5	0.5	nsec
Pump laser detuning	$\Delta$	5	5	$\Gamma_e^{(tot)}$
Two-photon detuning	$\delta$	0	0	$\Gamma_e^{(tot)}$

(Values are all in the laboratory frame.)

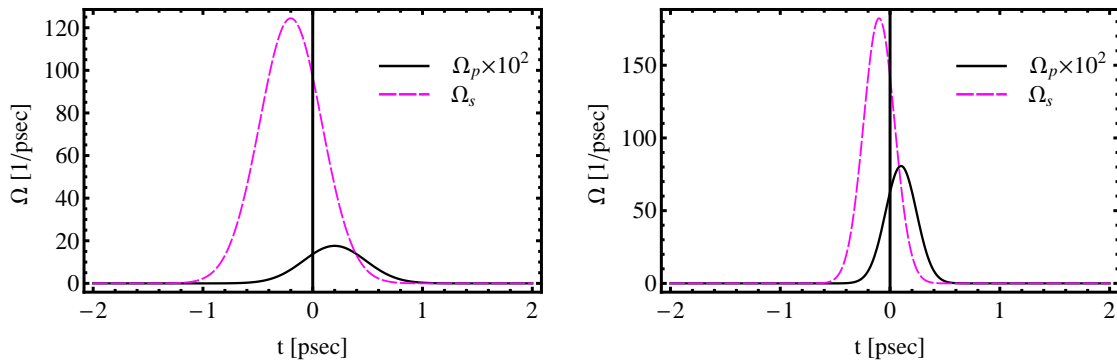


Figure 4: Rabi frequency profiles vs time  $t$  in the ion-at-rest frame for Kr (left) and Xe (right). The pump ( $\times 10^2$ , in black solid) and Stokes (in red dashed). See Table 5 for the parameters used.

### 3.2. Main simulation results

We now show our simulation results using Kr ions as a prime example. Figure 5 (left) shows time variation of populations of the excited state  $|e\rangle$ , the final state  $|f\rangle$ , and the state  $|1\rangle = |2^3S_1\rangle$ . Note that  $t$  in this figure (and also the following figures) represents the time in the ion-at-rest frame. As seen, a sizable fraction is transported to  $|f\rangle$  although excitation to  $|e\rangle$  is non-negligible. The intermediate state  $|1\rangle$  increases gradually because it is mainly generated through  $|f\rangle$ . See Figure 2 and/or Table 4. The decay from  $|f\rangle$  to the ground state  $|g\rangle$  occurs quickly, and gives the twisted gamma-rays (signal events). Figure 5 (right) shows the time variation of the other populations,  $|2\rangle \sim |5\rangle$ : they are found to be at least two order of magnitude smaller than that of  $|f\rangle$ .

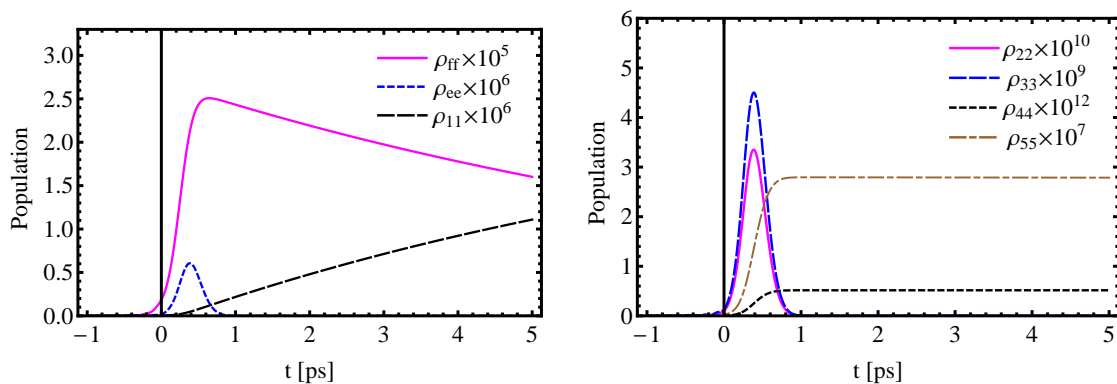


Figure 5: Variation of populations as a function of time  $t$  in the ion-at-rest frame (Kr). (left)  $\rho_{ff} \times 10^5$  (solid magenta),  $\rho_{11} \times 10^6$  (dashed black),  $\rho_{ee} \times 10^6$  (dotted blue). (right)  $\rho_{22} \times 10^{10}$  (solid magenta),  $\rho_{33} \times 10^9$  (dashed blue),  $\rho_{44} \times 10^{12}$  (dotted black),  $\rho_{55} \times 10^7$  (dash-dotted brown). See Table 5 (Kr) for the parameters used.

Now we discuss about more important quantities such as signal or background production probability (or “event rate” for simplicity). The solid magenta line in Figure 6 shows the probability of signal events integrated up to time  $t$ . It increases gradually with a time constant nearly equal to the lifetime of  $|f\rangle$ . Photons from the intermediate states  $|1\rangle \sim |5\rangle$  decaying to the ground state  $|g\rangle$  have similar energies with the signal, and may constitute undesirable background events (though it depends on actual experimental conditions). The dashed black line in Figure 6 shows the total probability summed over all contributions from  $|1\rangle \sim |5\rangle$  †. A step-function-like increase near  $t = 0$  is due the short-lived states of  $|2\rangle = |2^1P_1\rangle$  and  $|3\rangle = |2^3P_1\rangle$  while more gradual increase is mainly by  $|1\rangle$ . Note that since  $|1\rangle$  has a longer life time than  $|f\rangle$ , it is still increasing at  $t = 40$  psec. If we can bend the ion beam in the accelerator quickly enough, some of these background events would be directed away from an experimental area. In this paper, we evaluate the background events (and also the signal) at  $t = 40$  psec: this choice assumes that a bending section starts at 30 m downstream of the interaction (straight) section in the laboratory. With this definition, the signal and background rates are about  $2.3 \times 10^{-5}$  and  $1.3 \times 10^{-6}$ , respectively, giving the background-to-signal ratio ( $B/S$ ) of 5.6%.

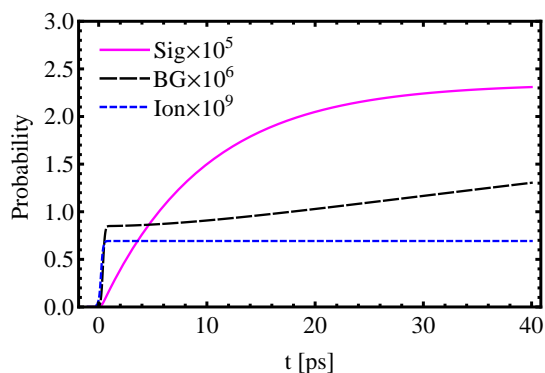


Figure 6: Event probability integrated up to time  $t$ . Signal ( $\times 10^5$ , solid magenta), background ( $\times 10^6$ , dashed black), and ionization ( $\times 10^9$ , dotted blue). See Table 5 (Kr) for the parameters used.

We next consider a photo-ionization effect, which is potentially serious because once ions are ionized (forming H-like ions) they are most likely lost from the accelerator. The dotted blue line in Figure 6 shows probability of photo-ionization loss summed over all possible channels. We see the loss rate amounts to  $6.9 \times 10^{-10}$ , which is found to be dominated by  $\sigma_{es}^{(pi)}$ , the photo-ionization process from  $|e\rangle$  by the Stokes laser photons. Whether this value is tolerable or not depends on an employed acceleration scheme. To get a feeling, we assume that it takes  $10^{-4}$  sec for the ions to circle around the accelerator

† A direct decay from  $|e\rangle$  to  $|g\rangle$  is another source of backgrounds. It is neglected, however, because its contribution is less than  $10^{-3}$  of those mentioned above. In addition, the resultant  $\gamma$ -ray energy differs significantly from that of the signal.

ring (*i.e.* its circumference is  $C_{ring} = 30$  km). Then the lifetime of ion beam due to this effect is about  $1.4 \times 10^5$  sec: this seems long enough to prepare a fresh bunch of ions.

### 3.3. Dependence on crucial parameters

In this section we will study the dependence of the signal and background rate on crucial parameters such as laser intensity, detuning or delay time. In all studies below, the He-like Kr is used and only one parameter is varied at a time.

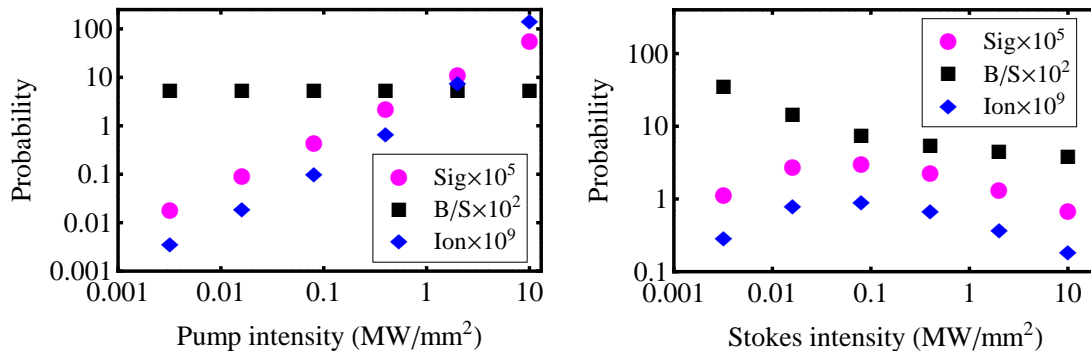


Figure 7: Input power dependence of pump (left) and Stokes (right) lasers. Symbols: signal rate ( $\times 10^5$ , circle in magenta), B/S ratio ( $\times 10^2$ , square in black), ionization rate ( $\times 10^9$ , diamond in blue).

Figure 7 (left) shows the pump laser intensity dependence of the signal rate ( $\times 10^5$ , circle in magenta), the background-to-signal ratio ( $\times 10^2$ , square in black), and the ionization rate ( $\times 10^9$ , diamond in blue). As seen, in the range we studied, the signal rate increases linearly with the input power while  $B/S$  remains constant. The ionization rate also increases with the input power but its dependence is faster than linear, and the probability reaches  $\sim 10^{-7}$  at  $I_p(0) = 10$  MW/mm<sup>2</sup> (the right most point), leading to a beam lifetime of  $\sim 1000$  sec. Figure 7 (right) shows a similar plot in case of the Stokes laser intensity. One notable feature is that  $B/S$  decreases monotonically with the laser power, but the signal rate peaks around  $I_s(0) \simeq 0.1$  MW/mm<sup>2</sup>. The latter feature is caused by an AC Stark effect (light shift): this is confirmed by a two-photon detuning study (see below).

Figure 8 (left) shows the pump laser detuning ( $\Delta$ ) dependence. As seen, all quantities decrease monotonically with  $\Delta$ . At  $\Delta = 0$ , the signal increases by a factor of 5, but  $B/S$  goes up to  $\sim 24\%$ . Figure 8 (right) shows a similar plot for two-photon detuning ( $\delta$ ). As seen, the signal rate peaks at around  $\delta \simeq 1 \times \Gamma_1^{(tot)}$ . The phenomenon can be understood as follows. It is well known that energy levels may be affected by the AC Stark effect [52, 53]. In the present case, it is suffice to consider the  $|e\rangle$  and  $|f\rangle$  two-level system since  $\Omega_p$  is much smaller than  $\Omega_s$ . The lower state level ( $|f\rangle$ ) would be shifted by  $\sim \Omega_s^2/(4\Delta)$ : thus the actual two-photon resonance condition becomes

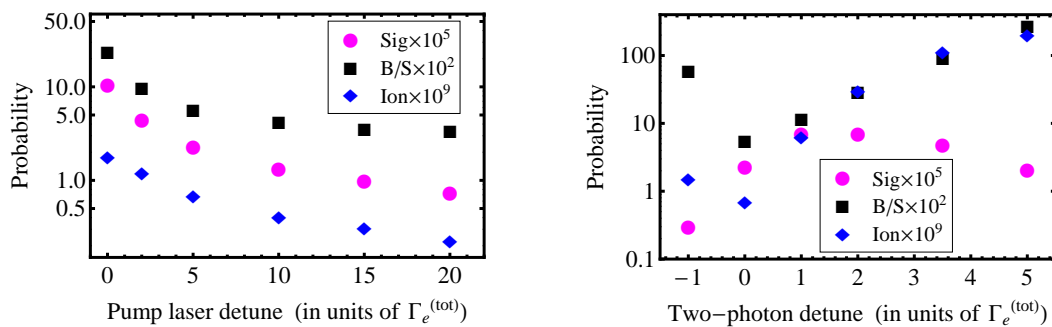


Figure 8: Detuning dependence of pump laser ( $\Delta$ , left) and two-photon ( $\delta$ , right). See the caption of Figure 7 for the symbols.

$\delta_{AC} = \omega_p - \omega_s - (\omega_{fg} + \Omega_s^2/(4\Delta))$ , instead of Equation (2). We expect the signal rate is largest when  $\delta_{AC} = 0$ , or  $\delta = \Omega_s^2/(4\Delta)$ . In the present case, taking  $\Omega_s \sim 60 \text{ ps}^{-1}$  (see Figure 4) and  $\Delta = 5 \times \Gamma_e^{(tot)}$ , we find  $\delta \simeq 1.3 \times \Gamma_e^{(tot)}$ , in rough agreement with the results shown in Figure 8 (right). Although the signal rate increases significantly with  $\delta$ , B/S also increases rapidly. Thus the choice of  $\delta$  must be made considering actual experimental requirements.

Finally the laser delay time dependence is studied as shown in Figure 9. The signal rate dependence shows a broad peak structure while the B/S ratio has a dip at around  $t_d = 0.25 \text{ nsec}$ .

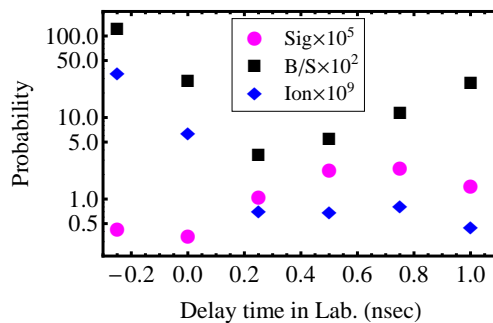


Figure 9: Delay time dependence. See the caption of Figure 7 for the symbols.

### 3.4. Comparison between Xe and Kr

We now turn our attention to Xe ions. Figure 10 shows time variation of populations. As anticipated, populations decay more quickly than Kr. Figure 11 shows the probabilities of signal, background, and ionization loss integrated up to time  $t$ . In this case, the event rate is defined at  $t = 20 \text{ psec}$ , considering  $\gamma_{ion}$  for Xe is twice as large as that for Kr. We find the signal and background rates are about  $5.8 \times 10^{-5}$  and  $1.1 \times 10^{-5}$ , respectively, giving the background-to-signal ratio of 19.2% while the ionization loss rate is about

$1.1 \times 10^{-9}$ . The most significant difference between Xe and Kr is the resulting gamma-ray energies; 306 MeV for Xe and 65.4 MeV for Kr. Incidentally, we note that there exists interesting difference between Xe and Kr in their signal and/or background time profile. See Figure 6 and Figure 11. In the case of Xe, the signal appears within a few psec after colliding with laser photons while the backgrounds grow more slowly. More or less the opposite is true in the case of Kr. This feature may be utilized in experiments to study differences or characters of the signal and backgrounds.

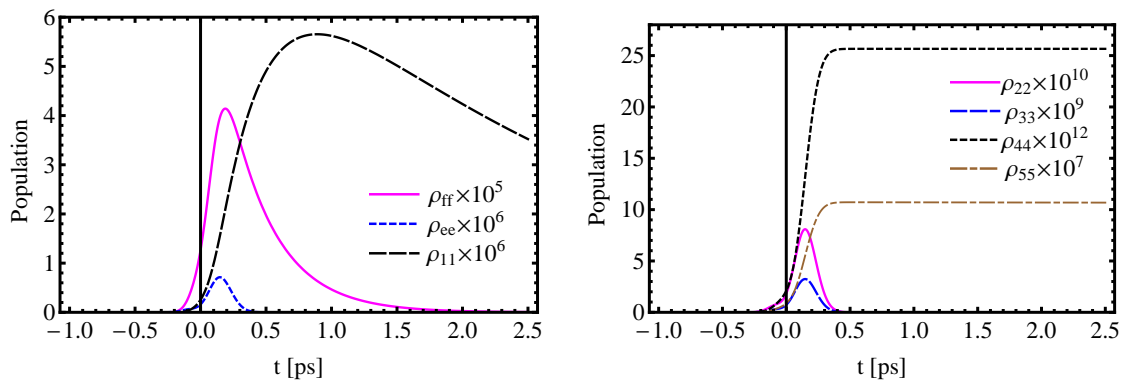


Figure 10: Variation of populations as a function of time  $t$  in the ion-at-rest frame (Xe). See Figure 5 for the symbols, and Table 5 (Xe) for the parameters used.

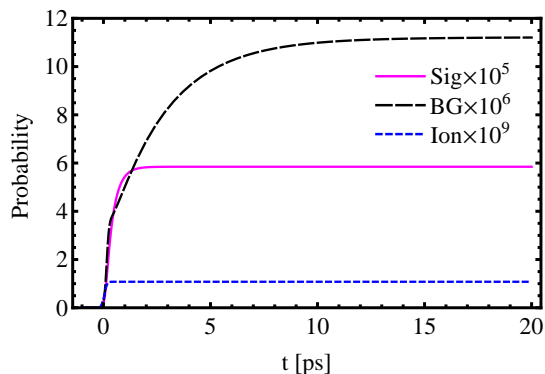


Figure 11: Event probability integrated up to time  $t$ . See the caption of Figure 6 for the symbols, and Table 5 (Xe) for the parameters used.

#### 4. Discussions and Summary

In this paper, we presented a new method of generating high-energy gamma rays with orbital angular momentum (OAM). It utilizes partially-stripped ions (PSIs) as an energy converter: accelerated PSIs absorb two photons and emit a photon with OAM. When initial PSIs have Lorentz boost factor of  $\gamma_{ion}$ , then the frequency of photons emitted

in the backward direction is up shifted in the laboratory to  $4\gamma_{ion}^2$  times the frequency difference of the two lasers. One important feature of the proposed method is use of a decay process from an excited state with quantum number  $J = 2$ ,  $M = 2$  to a ground state with  $J = 0$ ,  $M = 0$ . Thus emitted photons have an angular momentum  $M_\gamma = 2$  along the quantization axis (the beam axis). An actual scenario of the method is (below the values in the parentheses are those for Xe):

- (i) Ions: We select He-like Kr (Xe) ions as an energy converter, and populate the  $|2^3P_2\rangle$  excited state with the magnetic quantum number  $M = 2$ . Its major decay mode is M2-type radiative transition to the ground state: thus emitted photons have an angular momentum of  $M_\gamma = 2$ .
- (ii) Accelerator: We assume ions are accelerated up to  $\gamma_{ion} = 2500$  ( $\gamma_{ion} = 5000$ ) in a circular accelerator. A bunched ion beam revolves with a frequency of  $10^4$  Hz around its circumference of  $C_{ring} = 30$  km.
- (iii) Lasers: Two lasers, pump and Stokes, are injected to the ions to realize STIRAP-type population transfer. Their laboratory wavelengths are, respectively, 403 nm and 2690 nm (346 nm and 2371 nm). We assume a laser intensity of 400kW/mm<sup>2</sup> for each. See Table 5 for other parameters.

In order to study a signal rate as well as other important features, a set of equations (optical Bloch equations) are solved numerically. The main findings are as follows.

- (i) Signal: The signal gamma-ray has an energy of 65.4 MeV (305.9 MeV) in the laboratory, and its rate amounts to  $2.3 \times 10^{-5}$  ( $5.8 \times 10^{-5}$ ). Assuming that there are  $10^9$  ions in a bunch, the signal yield is  $2.3 \times 10^8$  Hz ( $5.8 \times 10^8$  Hz). If multiple bunches are put in an accelerator ring, then the yield increases accordingly.
- (ii) Background: Background gamma-rays stem from radiative decays from other  $n = 2$  states, and they have energies of 64.9, 65.6, and 65.1 MeV (301.3, 306.3, and 302.0 MeV), similar to the signal. The background-to-signal ratio ( $B/S$ ) is found to be 5.6% (19.2%). We note that the time profile of the signal and backgrounds differ significantly (see Figure 6 or Figure 11). Such difference may be utilized to discriminate the signal from backgrounds, for example, by comparing between early and later parts of gamma-ray pulses.
- (iii) Ionization loss: Photo-ionization effect might lead to loss of ions in an accelerator ring. In the present case, the loss rate is found to be about  $6.9 \times 10^{-10}$  ( $1.1 \times 10^{-9}$ ). We conclude that the beam lifetime due to this effect is long enough to prepare a fresh beam.
- (iv) Parameter dependence: We studied various parameter dependences of the signal rate and  $B/S$ . See section 3.3 for details. There are several ways to increase the signal rate further, but usually  $B/S$  deteriorates at the same time. Thus parameters must be chosen based on experimental requirements. One exception is the pump laser intensity: in this case the signal rate increases linearly with the input power while keeping  $B/S$  constant.

Finally, we make several comments below. First, we note that it is possible in principle to choose the  $|3^3P_1\rangle$  state as  $|e\rangle$ . In this case, the states  $|g\rangle$  and  $|e\rangle$  are connected by the E1 transition while  $|e\rangle$  and  $|f\rangle$  by the E2 transition. Unfortunately, there are several disadvantages in this scheme: the  $B/S$  ratio and ionization rate become much larger in order to obtain a similar level of the signal rate. In addition, the Stokes laser requires higher intensity.

Up to now we have treated rather an idealized ion beam because the main purpose of the present paper is to point out the basic principle. In ref. [54], some representative parameters of the gamma factory are shown. One important parameter is the ion beam energy spread ( $\Delta\gamma_{ion}/\gamma_{ion} = 10^{-4}$ ), which may reduce the signal gamma-ray production rate. It is expected that the spread in energy would cause the spread in two-photon detuning  $\delta$ . From Figure 8 (right), we find that the signal rates in the range  $0 - 5 \times \Gamma_e^{(tot)}$  is equal to or larger than that of  $\delta = 0$ . A very rough estimate of signal reduction factor is given by the effective width of  $\delta$  above divided by the energy spread of  $|f\rangle$ ,  $\hbar\omega_{fg} \times (\Delta\gamma_{ion}/\gamma_{ion})$ . This turns out to be  $\sim 3 \times 10^{-2}$ . Admittedly we need much more detailed analysis or simulation which includes various beam parameters in more detail. Another important beam parameters are the transverse beam size and the number of bunches in the ring; they are quoted as  $16 \mu\text{m}$  in radius, and  $592 - 1232$ , respectively, in ref. [54]. Those parameters affect significantly requirements on the lasers, and their feasibility must be studied more carefully. In any case, such studies are beyond the scope of this paper.

In summary, the proposed method offers an efficient way to produce intense gamma rays with orbital angular momentum. We hope such a beam would open up new opportunities for a variety of research fields.

## Acknowledgments

Part of the computation was performed using Research Center for Computational Science, Okazaki, Japan (Project: 21-IMS-C151). MoT was supported by the Inoue Enryo Memorial Grant (Toyo University). The work of NS is supported in part by JSPS KAKENHI Grant Number JP 16H02136. The work of MiT is supported in part by JSPS KAKENHI Grant Numbers JP 18K03621, 21H00074, and 21H00168.



## Appendix

In this Appendix, we explain how to deduce  $\Omega_p$  and  $\Omega_s$  from A coefficients. We use the Gauss unit system below, which is indicated by the subscript  $G$ .

In general, the total E1 (M1) decay rate from  $|J_1\rangle$  to  $|J_2\rangle$  (from  $|J_1\rangle$  to  $|J_0\rangle$ ) is given by [55]

$$\begin{aligned} A^{(E1)} &= \frac{4k^3}{3\hbar} \frac{1}{2J_1+1} \left| \langle J_1 || \vec{d}_G || J_2 \rangle \right|^2 \\ A^{(M1)} &= \frac{4k^3}{3\hbar} \frac{1}{2J_1+1} \left| \langle J_1 || \vec{m}_G || J_0 \rangle \right|^2 \end{aligned} \quad (8)$$

where  $k$  denotes the wavenumber corresponding to the transition, and  $\langle J_1 || \vec{d}_G || J_2 \rangle$  ( $\langle J_1 || \vec{m}_G || J_0 \rangle$ ) is the reduced matrix element of the electric dipole moment  $\vec{d}_G = e_G \vec{r}$  (the magnetic dipole moment  $\vec{m}_G = \frac{e_G \hbar}{2m_e} (\vec{L} + 2\vec{S})$ ). The Rabi frequency via E1 (M1) transition, connecting the state  $|J_1 M_1\rangle$  and  $|J_2 M_2\rangle$  ( $|J_0 M_0\rangle$  and  $|J_1 M_1\rangle$ ), is expressed by

$$\begin{aligned} \Omega_R^{(E1)} &= \frac{\langle J_2 M_2 | \vec{d}_G \cdot \vec{E}_G | J_1 M_1 \rangle}{\hbar} = \frac{E_{G0}}{\hbar} \langle J_2 M_2 | d_G^q | J_1 M_1 \rangle \\ \Omega_R^{(M1)} &= \frac{\langle J_1 M_1 | \vec{m}_G \cdot \vec{B} | J_0 M_0 \rangle}{\hbar} = \frac{B_{G0}}{\hbar} \langle J_1 M_1 | m_G^q | J_0 M_0 \rangle \end{aligned} \quad (9)$$

where  $d_G^q$  ( $m_G^q$ ) denotes the  $q$ -th ( $q = \pm 1$ ) component of the dipole operator, and  $\vec{E}_G$  ( $\vec{B}_G$ ) is the electric (magnetic) field having a polarization  $\vec{\epsilon}_q$  and magnitude  $E_{G0}$  ( $B_{G0}$ ). Note that  $q$  ( $-q$ ) indicates the circular polarization of absorbed (emitted) photon by  $|J_1, M_1\rangle$  or  $|J_0, M_0\rangle$ . The individual matrix element above and the reduced matrix element are related each other by the Wigner-Eckart theorem [55]:

$$\begin{aligned} \langle J_2 M_2 | d_G^q | J_1 M_1 \rangle &= \frac{1}{\sqrt{2J_2+1}} \langle J_2 || d_G || J_1 \rangle C(J_1 M_1, 1q; J_2 M_2), \\ \langle J_1 M_1 | m_G^q | J_0 M_0 \rangle &= \frac{1}{\sqrt{2J_1+1}} \langle J_1 || m_G || J_0 \rangle C(J_0 M_0, 1q; J_1 M_1), \end{aligned} \quad (10)$$

where  $C(J_1 M_1, 1q; J_2 M_2)$  and  $C(J_0 M_0, 1q; J_1 M_1)$  are the Clebsch-Gordan coefficients. We now combine Equation (8), (9) and (10), and, in the present case, set  $q = 1$ ,  $J_0 = M_0 = 0$ ,  $J_1 = M_1 = 1$ , and  $J_2 = M_2 = 2$ . Inserting  $C(00, 11; 11) = C(11, 11; 22) = 1$ , we finally arrive at the relations

$$\Omega_R^{(E1)} = E_{G0} \sqrt{\frac{9 A^{(E1)}}{20 \hbar k^3}}, \quad \text{and} \quad \Omega_R^{(M1)} = B_{G0} \sqrt{\frac{3 A^{(M1)}}{4 \hbar k^3}}. \quad (11)$$

Note that irrelevant phase factors are omitted above, and that the choice of  $q = 1$  means the right-circular polarization for the pump (absorbed) and left-circular polarization for the Stokes (emitted). In order to express Equation (11) by quantities in the SI units, we use the conversion rule [56],  $E_{G0} = B_{G0} = \sqrt{4\pi\epsilon_0} E_0$  ( $\epsilon_0$  being the permittivity of free space), along with the fine structure constant  $\alpha = \frac{e_G^2}{\hbar c} = \frac{e^2}{4\pi\epsilon_0 \hbar c}$ .

## References

- [1] V.B. Berestetskii, E.M. Lifshitz and L.P. Pitaevskii, “Quantum Electrodynamics”, 2nd Edition, 1980, Pergamon Press, Oxford.
- [2] L. Allen, et al. “Orbital angular momentum of light and the transformation of Laguerre-Gaussian laser modes.” *Phys. Rev. A* 45, 8185–8189 (1992).
- [3] Shen et al. “Optical vortices 30 years on: OAM manipulation from topological charge to multiple singularities”, *Light: Science & Applications* 8 :90 (2019) <https://doi.org/10.1038/s41377-019-0194-2>
- [4] M. J. Padgett, “Orbital angular momentum 25 years on”, *Opt. Express* 25(10), 11265–11274 (2017).
- [5] G. Molina-Terriza, J. P. Torres and L. Torner, “Twisted photons”. *Nat. Phys.* 3, 305–310 (2007).
- [6] “Twisted photons”, Edited by J.P.Torres and L.Torner, Wiley-VCH Weinheim, Germany, 2011; ISBN:978-3-527-40907-5
- [7] Mohamed Babiker, David L Andrews and Vassilis E Lembessis, “Atoms in complex twisted light”, *J. Opt.* 21 (2019) 013001
- [8] Maria Solyanik-Gorgone, Andrei Afanasev, Carl E. Carlson, Christian T. Schmiegelow, Ferdinand Schmidt-Kaler, “Excitation of E1-forbidden atomic transitions with electric, magnetic, or mixed multipolarity in light fields carrying orbital and spin angular momentum”, *Journal of the Optical Society of America B*, 36, 565 (2019)
- [9] A. Mair, A. Vaziri, G. Weihs, and A. Zeilinger, “Entanglement of the orbital angular momentum states of photons”, *Nature* 412(6844), 313-316 (2001).
- [10] J. Leach, B. Jack, J. Romero, M. Ritsch-Marte, R. W. Boyd, A. K. Jha, S. M. Barnett, S. Franke-Arnold, and M. J. Padgett, “Violation of a Bell inequality in two-dimensional orbital angular momentum state-spaces”, *Opt. Express* 17(10), 8287–8293 (2009).
- [11] H. He, M. E. J. Friese, N. R. Heckenberg, and H. Rubinsztein-Dunlop, “Direct observation of transfer of angular momentum to absorptive particles from a laser beam with a phase singularity”, *Phys. Rev. Lett.* 75(5), 826–829 (1995).
- [12] V. Garcés-Chávez, D. McGloin, M.J. Padgett, W. Dultz, H. Schmitzer, K. Dholakia, “Observation of the transfer of the local angular momentum density of a multiringed light beam to an optically trapped particle”, *Phys Rev Lett.* 2003 Aug 29;91(9):093602. doi: 10.1103/PhysRevLett.91.093602. Epub 2003 Aug 29. PMID: 14525181.
- [13] G. A. Swartzlander, “Peering into darkness with a vortex spatial filter”, *Opt. Lett.* 26(8), 497–499 (2001).
- [14] G. A. Swartzlander, Jr., E. L. Ford, R. S. Abdul-Malik, L. M. Close, M. A. Peters, D. M. Palacios, and D. W. Wilson, “Astronomical demonstration of an optical vortex coronagraph”, *Opt. Express* 16(14), 10200–10207 (2008).
- [15] S. Fürhapter, A. Jesacher, S. Bernet, and M. Ritsch-Marte, “Spiral interferometry,” *Opt. Lett.* 30(15), 1953–1955 (2005).
- [16] Manuel Erhard, Robert Fickler, Mario Krenn and Anton Zeilinger, “Twisted photons: new quantum perspectives in high dimensions”, *Light: Science & Applications* (2018) 7, 17146; doi:10.1038/lsa.2017.146
- [17] Graham Gibson, Johannes Courtial, Miles J. Padgett, Mikhail Vasnetsov, Valeriy Pas’ko, Stephen M. Barnett, Sonja Franke-Arnold, “Free-space information transfer using light beams carrying orbital angular momentum”, *Opt. Express* 12(22), 5448–5456 (2004)
- [18] M. Krenn, J. Handsteiner, M. Fink, R. Fickler, R. Ursin, M. Malik, and A. Zeilinger, “Twisted light transmission over 143 km”, *Proc. Natl. Acad. Sci. U.S.A.* 113(48), 13648–13653 (2016).
- [19] M. Harwit, “Photon orbital angular momentum in astrophysics.”, *Astrophys. J.* 597, 1266-1270 (2003).
- [20] Fabrizio Tamburini, Bo Thide and Massimo Della Valle, “Measurement of the spin of the M87 black hole from its observed twisted light”, *MNRAS* 492, L22–L27 (2020) doi:10.1093/mnras/slz176
- [21] T. Maruyama, T. Hayakawa, T. Kajino and M. K. Cheoun, “Generation of photon vortex by

- synchrotron radiation from electrons in Landau states under astrophysical magnetic fields”, *Phys. Lett. B* **826**, 136779 (2022) doi:10.1016/j.physletb.2021.136779
- [22] Xuewen Wang, Zhongquan Nie, Yao Liang, Jian Wang, Tao Li and Baohua Jia, ”Recent advances on optical vortex generation”, *Nanophotonics* 2018; 7(9): 1533–1556
- [23] M.W. Beijersbergen, L. Allen, H.E.L.O. van der Veen and J.P. Woerdman , ”Astigmatic laser mode converters and transfer of orbital angular momentum”, *Optics Communications* 96 (1993) 123-132
- [24] L. Marrucci, C. Manzo, and D. Paparo, “Optical spin-to-orbital angular momentum conversion in inhomogeneous anisotropic media”, *Phys. Rev. Lett.* 96(16), 163905 (2006)
- [25] S. Sasaki and I. McNulty, “Proposal for generating brilliant x-ray beams carrying orbital angular momentum”, *Phys. Rev. Lett.* 100(12), 124801 (2008).
- [26] J. Bahrdt, K. Holldack, P. Kuske, R. Müller, M. Scheer, and P. Schmid, “First Observation of Photons Carrying Orbital Angular Momentum in Undulator Radiation”, *Phys. Rev. Lett.* 111, 034801 (2013).
- [27] Kaneyasu Tatsuo, Hikosaka Yasumasa, Fujimoto Masaki, Iwayama Hiroshi, Hosaka Masahito, Shigemasa Eiji, Katoh Masahiro, “Observation of an optical vortex beam from a helical undulator in the XUV region”, *JOURNAL OF SYNCHROTRON RADIATION*, 24, 934-938, (2017)
- [28] E. Hemsing, A. Knyazik, F. O’Shea, A. Marinelli, P. Musumeci, O. Williams, S. Tochitsky, and J. B. Rosenzweig, “Experimental observation of helical microbunching of a relativistic electron beam”, *Appl. Phys. Lett.* 100, 091110 (2012); <https://doi.org/10.1063/1.3690900>
- [29] E. Hemsing, A. Knyazik, M. Dunning, D. Xiang, A. Marinelli, C. Hast, and J. B. Rosenzweig, “Coherent optical vortices from relativistic electron beams”, *Nat. Phys.* 9(9), 549 (2013).
- [30] P. R. Ribic, B. Rösner, D. Gauthier, E. Allaria, F. Döring, L. Foglia, L. Giannessi, N. Mahne, M. Manfredda, C. Masciovecchio et al., “Extreme-ultraviolet vortices from a free-electron laser”, *Phys. Rev. X* 7(3), 031036 (2017).
- [31] U. D. Jentschura and V. G. Serbo, “Generation of high-energy photons with large orbital angular momentum by Compton backscattering”, *Phys. Rev. Lett.* 106(1), 013001 (2011).
- [32] U. D. Jentschura and V. G. Serbo, “Compton upconversion of twisted photons: Backscattering of particles with non-planar wave functions”, *Eur. Phys. J. C* 71(3), 1571 (2011).
- [33] I. Ivanov and V. Serbo, “Scattering of twisted particles: Extension to wave packets and orbital helicity”, *Phys. Rev. A* 84(3), 033804 (2011).
- [34] S. Stock, A. Surzhykov, S. Fritzsche, and D. Seipt, “Compton scattering of twisted light: Angular distribution and polarization of scattered photons”, *Phys. Rev. A* 92(1), 013401 (2015).
- [35] V. Petrillo, G. Dattoli, I. Drebot, and F. Nguyen, “Compton scattered xgamma rays with orbital momentum”, *Phys. Rev. Lett.* 117(12), 123903 (2016).
- [36] Y. Taira, T. Hayakawa, and M. Katoh, “Gamma-ray vortices from nonlinear inverse Thomson scattering of circularly polarized light”, *Sci. Rep.* 7(1), 5018 (2017).
- [37] Yue-Yue Chen, Karen Z. Hatsagortsyan, and Christoph H. Keitel, ”Generation of twisted  $\gamma$ -ray radiation by nonlinear Thomson scattering of twisted light”, *Matter Radiat. Extremes* 4, 024401 (2019); <https://doi.org/10.1063/1.5086347>
- [38] D. Budker *et al.*, *Ann. Phys. (Berlin)* 532 (2020) 2000204.
- [39] M. Tanaka and N. Sasao, *Int. J. Mod. Phys. E* 30, (2021) 2150040.
- [40] Valeriy G. Serbo, Andrey Surzhykov, and Andrey Volotka, *Ann. Phys. (Berlin)* 534, (2022) 2100199; <https://doi.org/10.1002/andp.202100199>
- [41] E.G Bessonov, *Nucl. Instr. Meth. B* 309, 92 (2013).
- [42] M.W. Krasny, “Gamma Factory, Proof-of-Principle Experiment”, CERN-SPSC-2019-031; SPSC-I-253.
- [43] P. Ivanov, “Colliding particles carrying nonzero orbital angular momentum”, *Phys. Rev. D* 83(9), 093001 (2011)
- [44] N. V. Vitanov *et al.*, *Rev. Mod. Phys.* 89, (2017) 015006.

- [45] I. I. Sobelman, “Atomic Spectra and Radiative Transitions”, (Springer, Hederberg 1992).
- [46] C. D. Lin, R. Johnson, and A. Dalgarno, Phys. Rev. A 15, (1977), 154.
- [47] I.P. Grant, *Relativistic Quantum Theory of Atoms and Molecules*, Springer, New York (2007).
- [48] C. Froese Fischer, G. Gaigalas, P. Jönsson and J. Bieron, Comput. Phys. Commun. **237**, 184 (2019).
- [49] P.J. Mohr, G. Plunien, and G. Soff, Phys. Rept. **293**, 227 (1998).
- [50] S. Fritzsche, Comput. Phys. Commun. **183**, 1525 (2012).
- [51] G. Lindblad, Commun. Math. Phys. **48** 119 (1976).
- [52] C. Cohen-Tannoudji and D. Guery-Odelin, *Advances in Atomic Physics* (World Scientific, Singapore 2011) page-148.
- [53] C. J. Foot, *Atomic Physics* (Oxford University Press, Oxford 2005) page-144.
- [54] D. Budker *et al.*, Ann. Phys.(Berlin) 534 (2022), 2100284
- [55] A. Messiah, *Quantum Mechanics, Two Volumes Bound as One* (Dover, 1999) page-1045, 1052 and 573.
- [56] J. D. Jackson, *Classical Electrodynamics* (Wiley, 1999) page-782